SunKrist Publishing
Accelerate Scientific Knowledge in Open Access

SunKrist Nanotechnology and Nanoscience Journal

Research Article *Volume: 1, Issue: 1* *Scientific Knowledge*

First Insight on Electronic Structure, Structural Stability, Dynamical and Mechanical Properties of Two-Dimensional $LaAuo_3$

P Vajeeston,[1*] F Bianchini,[1] M Rasukkannu[2] and H Fjellvåg[1]

[1]Department of Chemistry, Center for Materials Sciences and Nanotechnology, University of Oslo, Norway.

[2]Department of Computing, Western Norway University of Applied Sciences, Norway

1.Abstract

The electronic structure, structural stability, dynamical, mechanical, ionic conductivity, optical properties and bonding nature of $LaAuO_3$ are investigated by means of first principle calculations based on density functional theory (DFT). The equilibrium structural parameters are obtained within the general gradient approximation (GGA), in particular using the Perdew Burke Ernzerhof (PBE) exchange correlation functional, while the electronic structure is investigated using the screened hybrid functional proposed by Heyd, Scuseria and Ernzerhof (HSE06). The computed band gaps values and the nature of the electronic structure are found to be similar to ZnO and GaN. The detailed chemical bonding analysis reveals the nature of bonds: La–O exhibit mainly ionic interaction, whereas Au–O exhibits iono-covalent interactions. This study provides a fundamental understanding of the structural, mechanical and electronic properties of $LaAuO_3$.

2. Introduction

Advanced theoretical-computational techniques, combined with the increasing power of computers, provide an understanding of matter at the atomic-scale with an unprecedented level of detail and accuracy. These calculations are not only capable of reproducing experimental data, they also allow for the design of novel materials and the prediction of their properties, thus providing a fundamental understanding, which would not require the synthesis of the target, compounds. The goal of these computational techniques is to simulate more materials in a more detailed fashion, including the interaction with the environment, depending on the computational cost and the overall accuracy of the technique. The last three decades have witnessed dramatic advances in condensed matter theory, driven, in large part, by new and sophisticated experiments on high-purity materials which have been thoroughly characterized [1]. In most areas of condensed matter theory and particularly in electronic structure, these advances may be attributed directly to the close intertwining between theoretical and experimental research. Indeed, the newfound ability to apply fundamental theoretical concepts to real materials (rather than to simple model systems) made possible by utilizing the continued rapid

*Corresponding author: P Vajeeston, Center for Materials Sciences and Nanotechnology, Department of Chemistry, University of Oslo, P.O. Box 1033 Blindern, N-0315 Oslo, Norway, E-mail: ponniahv@kjemi.uio.no **Received Date:** July 3, 2019; **Accepted Date:** July 15, 2019; **Published Date:** July 17, 2019

development of computer power, has served to fill the increasingly high demand of experimentalists for theoretical interpretation of their data. Also, in some cases these computational efforts can be used to provide data which would be impossible or impractical to obtain experimentally. The range and variety of materials under investigation is enormous. On the other hand, the experimental investigations are very limited due to several limitations (cost, work force, lack of phase-pure samples, etc.). However, a deeper and fundamental understanding of the properties of the materials is required for the prediction of any specific device application and improvements. Therefore, investigations of the structural, electronic, optical and elastic properties as well as understanding the overall characteristics of the system is utmost important. To the best of our knowledge, this compound is currently not thoroughly investigated in the literature, as only the crystal structure of the α-phase is known and virtually no other properties. However, Xiao et al. [2] found that, based on tight-binding modelling and first-principles calculations, bilayers of perovskite-type transition-metal oxides grown along the (111) crystallographic axis are potential candidates for two-dimensional topological insulators [3]. The topological band structure of these materials can be fine-tuned by changing dopant ions, substrates and external gate voltages. $LaAuO_3$ bilayers have a topologically non-trivial energy gap of about 0.15 eV, which is sufficiently large to realize the quantum spin Hall effect at room temperature. In this paper, we report on structural, dynamical and mechanical stability, ionic conductivity, electronic structure, chemical bonding, Raman, IR spectra and optical properties of $LaAuO_3$ polymorphs

3. Computational Details

Total energies have been calculated by the projected-augmented plane-wave (PAW) implementation of the Vienna ab initio simulation package (VASP) [4,5]. These calculations were performed using the Perdew, Burke and Ernzerhof (PBE) [6] exchange correlation functional. Ground-state geometries were determined by minimizing stresses and Hellman-Feynman forces using the conjugate-gradient algorithm with a force convergence threshold of 10^{-3}eV $Å^{-1}$. Brillouin zone integration was performed with a Gaussian broadening of 0.1 eV during all relaxations. From various sets of calculations, it was found that 1050 k points in the Brillouin zone for the $LaAuO_3$-type (Pbcm) structure and a 600 eV cut-off energy for the expansion into plane-waves are sufficient to ensure optimum accuracy (10^{-3}eV $Å^{-1}$) in the computed results. The k-points were generated using a Monkhorst-Pack 12×8×4 grid (for the $LaAuO_3$ in Pbcm structure) for structural optimization. A similar density of k-points and energy cut-off were used to estimate the total energy as a function of volume for all the structures considered in the present study.

The calculated total energy as a function of volume has been fitted to the universal equation of state (EOS) [7]. The transition pressures are calculated from the pressure vs. Gibbs free energy curves. The Gibbs free energy ($G = U+PV-TS$ where $T = 0$; G = total energy + pressure×volume) is calculated in the following way: The calculated volume verses total energy for two data sets were read in and for each data set the total energy and volume have been fitted to the universal EOS function. The pressure is defined as $P = (B_0/B_0') \times [(v_e/v)^{B0'} - 1]$, which gives volume ($v$) = $v_e / [(1 + (B_0'/ B_0 \times p)^{1/B0'}]$ where v_e, B_0 and $B_0|$ refers to the equilibrium volume, bulk modulus and derivative of bulk modulus, respectively. The inverse is then calculated using the bisection method. From the scan over the pressures, the corresponding difference in the enthalpy between the two data sets was calculated. A frozen phonon calculation was performed on supercells systems, as implemented in the phonopy program, to obtain the phonon dispersion curves and the associated density of states [8]. The

supercell size is chosen so that periodic images are separated by at least 12 Å for improved accuracy. An additional support FFT grid, 8 times denser than the regular one, is used for the evaluation of the augmentation charges, greatly reducing the noise in the Hellmann–Feynman forces. An atomic displacement of 0.0075 Å was used with symmetry considerations to obtain the force constants. The displacements in opposite directions along all the axes were incorporated to improve the precision of the calculation. The atomic forces were computed using the VASP code and the resulting data were imported into the Phonopy program. The dynamical matrices were calculated from the force constants and phonon Density of states (DOS) were integrated over a Monkhorst-Pack grid [9]. The thermal properties, such as heat capacity, free energy and entropy, were calculated using the thus obtained phonon DOS.

4. Result and discussion

In order to understand the relative stability of the $LaAuO_3$ chemical composition the following 12 structures are considered in the theoretical simulation, the space group, space group number and number of formula unit (Z) are given in parenthesis: $CaTiO_3$-type (*Pm*-3*m*; 221; Z = 1) ; $LaAuO_3$-type (Pbcm; 57; Z=4) ; $GdFeO_3$-type (Pnma; 62; Z = 4) ; $NdAlO_3$-type (R-3cH; 167, Z=6); $LaVO_3$-type ($P2_1/c$; 14; Z = 4) ; $CaTiO_3$ -type (Cmmm; 65; Z = 2) ; $PbTiO_3$-type (P4mm; 99; Z = 1) ; $BaTiO_3$-type (Amm2; 38; Z = 2) ; La_2CuSnO_6-type ($P2_1/m$; 11; Z = 4) ; $CaTiO_3$-type (C2/m; 12; Z = 8) ; $SrTiO_3$-type (I4/mcm; 140; Z = 4), and $BaFeO_{2+x}$ -type (P63/mmc; 194; Z =6) [10].

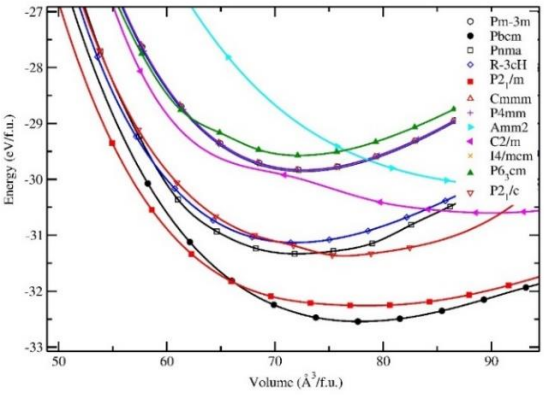

Figure 1: The calculated total energy as a function of volume for the different polymorphs of $LaAuO_3$. The associated space groups are labelled in the illustration.

4.1 Structural properties

The calculated total energies as a function of the unit cell volume for the studied phases are displayed in Figure 1. The $LaAuO_3$-type configuration (hereafter labelled α-$LaAuO_3$) is lower in energy than the other structures considered. The calculated structural parameters and atomic positions are in agreement with the experimental findings [11]. The crystal structure contains one crystallographic independent position for Au with site symmetry *m*. The coordination to oxygen is approximately square planar (Figure 1a), thus, unambiguously indicating gold to be trivalent. The mirror plane is oriented perpendicular to the plane formed by the oxide ions of the AuO_4 group. Similarly, lanthanum is located on a crystallographically independent position with site symmetry *m*. The La atom is coordinated to six O atoms, with bond lengths in the range 2.44-2.57 Å and to two O atoms with a 2.69 Å separation. These atoms, labelled O_1 and O_2, occupy the Wyckoff positions 8*e* and 4*c* respectively. The polyhedron formed is approximately cubic (Figure 2). In this structure, the mirror plane is oriented perpendicular to the edge of the cube connecting O_2 and O_2. The mean La-O bond length is in line with other structures containing La in an eight-fold site with approximately cubic coordination [12]. The AuO_4 squares are connected to each other via half of their vertices (O_2), while the LaO polyhedra are connected via edges (O_1) and vertices (O_2). The longer distance between Au and O_2 (as compared to O_1) is explicable by the higher bonding charge on O_2, which is connected to two gold atoms. O_1 is instead bonded only to one gold ion. The three-dimensional framework is dominated by a grid of cubes formed by the oxide ions. The next energetically favorable phase is La_2CuSnO_6-type derived *P*121/*m*1, (spg. nr.11) structure (hereafter labelled β-$LaAuO_3$).

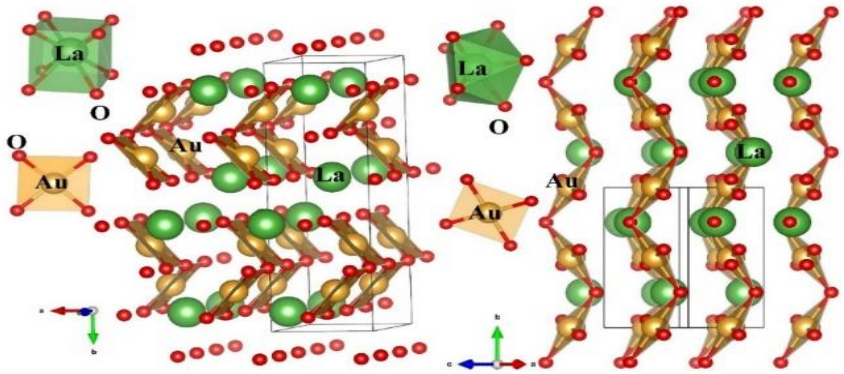

Figure 2: Theoretically predicted low energy crystal structures for $LaAuO_3$: (a) Pbcm structure and (b) $P121/m^1$ structure at equilibrium volume. The legends for the different kinds of atoms are given in the illustration.

The crystal structure of β-$LaAuO_3$ includes two formula units per unit cell. This modification presents 2 inequivalent oxygen sites, with Wyckoff labels and multiplicity 4*f* (O_1) and 2*e*(O_2). These atoms, indicated in Figure11, are coordinated by two Au and one La atoms, with bond lengths of 2.03 Å and 2.55 Å respectively. Six O_1 type atoms are coordinated by lanthanum, with bond lengths variable between 2.38 Å and 2.50 Å. The O_2 atom exhibits an equilibrium distance of 2.58 Å from the La site. Similarly, to the α-phase, the Au coordination by oxygen in β-$LaAuO_3$ is approximately square planar (Figure 2b), thus, unambiguously indicating gold to be trivalent. La is coordinates to 8 oxygen atoms. In contrast with the α-phase, the LaO_8 polyhedron is more distorted. This structure is completely different from the starting geometry. In the starting geometry the main structural feature that makes the crystal structure complex is the buckling of the AuO_2 planes. The involved energy difference between the two structures at the equilibrium is 282 meV/f.u. It is interesting to note that both of these two modifications exhibit similar unit cell volumes (77.97 and 78.08 $Å^3$/f.u. for α- and β-$LaAuO_3$, respectively) and at 1.98 GPa α- phase transforms into β-$LaAuO_3$.

Table 1: Crystallographic details of structures of the $LaAuO_3$ system. The experimentally observed values are reported in parenthesis.

Phase	**Space group**	***Z***	**Lattice parameters**	**Atomic sites**				
				Atom	**Wyk.pos.**	***x***	***y***	***z***
α-$LaAuO_3$	*Pbcm* (57)	4	*a* = 4.0708 (4.0335[a])Å	La	4*d*	0.2637(0.2643[a])	0.5806 (0.5823[a])	¼
			b=13.2703(13.0730[a])Å	Au	4*d*	0.0748 (0.0715[a])	0.3298 (3293[a])	¼
			c=5.7509 (5.6952[a]) Å	O_1	*8e*	0.2567 (0.2551[a])	0.4222(0.4204[a])	0.0039(0.0061[a])
				O_2	4*c*	0.8302 (0.8275[a])	¼	0
β-$LaAuO_3$	$P2_1/m$ (11)	2	*a* = 5.3886 Å	La	2e	0.0091	¼	0.7248
			b =6.9704 Å	Au	2*b*	½	½	0
			c=3.5208 Å	O_1	*4f*	0.1937	0.0547	0.2683
			β=94.09	O_2	2*e*	0.6619	¼	0.1821

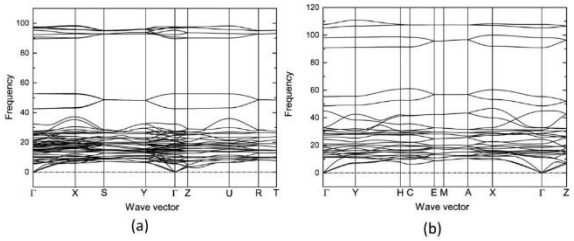

Figure 3: Calculated phonon dispersion curves for the α- phase at its equilibrium volume (left panel) and for the β- phase above the transition point (at 2 GPa).

4.2 Dynamical stability

In order to understand the dynamical stability of the α- and β- phases, we have also calculated phonon dispersion (PD) curves and phonon density of state (PhDOS) for α- at the equilibrium volume and β- phase at 2GPa, which are shown in Figure 3-5, respectively. From these figures, it is clear that these-modifications do not exhibit imaginary frequency, indicating that the experimentally known α-phase and the theoretically predicted β-phase are dynamically stable configurations [13]. As per the theory, the high pressure β-phase is found to be dynamically stable. As can be observed in Figure 3, the α- and β- modifications exhibit different PD and PhDOS due to the distinct structural arrangements. Owing to the two-dimensional structural arrangement, the calculated PD and PhDOS for both modifications are very narrow. The partial phonon DOS are displayed in Figure 4,5. The partial PhDOS for both α- and β- modifications are projected along the system axes. For La, Au and O atoms, the vibrational modes along the *x*, *y* and *z* directions are considerably different in the entire frequency region. Figure 4 and 5 shows that, for both α- and β- phases, the high frequency modes above 90 THz and the intermediate frequency regime (42 to 52THz for α-phase; and 48 to 61 THz for β-phase) are dominated by Au. In both phases, the low frequency modes below 15 THz are mainly dominated by O atom. The La modes in α- phase are present between 12 to 37 THz frequency range and for the β-phase the corresponding modes are present between 25 to 45 THz.

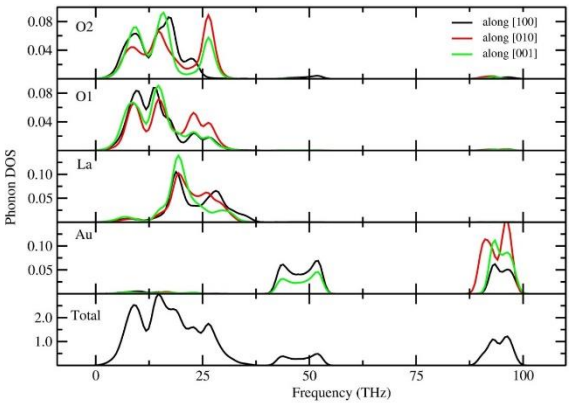

Figure 4: The calculated total, site and direction dependent phonon density of states for the α-$LaAuO_3$ at equilibrium volume.

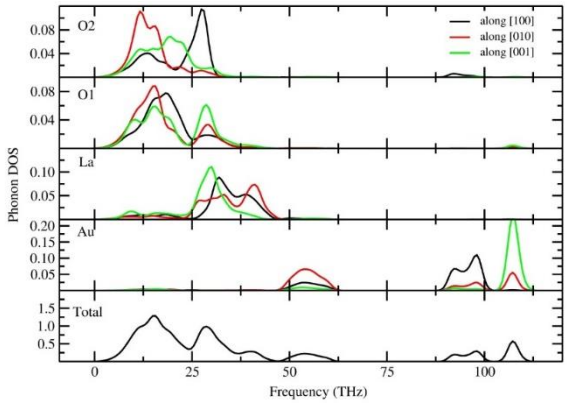

Figure 5: The calculated total, site and direction dependent phonon density of states for β- $LaAuO_3$ phases at 2 GPa.

In addition to dynamical stability, the thermodynamic properties of $LaAuO_3$ polymorphs, including free energy, entropy and lattice heat capacity) are calculated as a function of temperature and reported in Figure 6. these quantities exhibit different behaviours for α- and β- $LaAuO_3$. The specific heat coefficient increases rapidly below 400K. Above this temperature, the slope becomes gentler.

4.3 Single crystal elastic constants and mechanical stability

To understand the mechanical stability of the predicted structures, we have computed the elastic constants from linear response density functional perturbation theory calculations [12]. The elastic constants describe the response of the material to an applied stress or, conversely, the stress required to maintain a certain deformation. Both the stress and the strain tensors have three tensile and three shear components. When these quantities are expressed

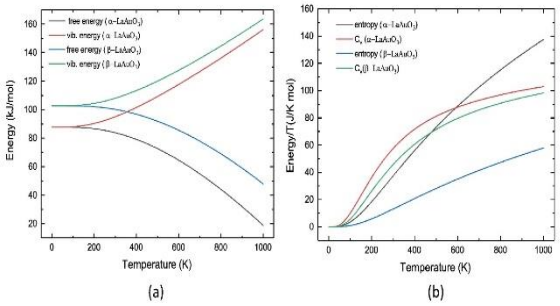

Figure 6: Calculated free energy (in kJ/mol), vibrational energy (in kJ/mol), entropy (in J/K mol.) and lattice heat capacity (Cv; in J/K mol.) as a function of temperature for $LaAuO_3$ polymorphs.

using the Voigt notation, the linear elastic constants are described by a 6×6 symmetric matrix with 21 independent elements. However, system symmetries can reduce considerably this number. Linear response perturbation theory has been successfully used to compute the elastic constants of a vast range of materials [including simple metals (such as Al) [14], super hard nitrides [15], borides [16, 17], oxides [18], silicates [19] and semiconductors [20,21], with a typical accuracy within 10% from experimental values [19].

Table 2: The calculated single crystal elastic constants C_{ij} (in GPa), bulk modulus B (in GPa), shear modulus G (in GPa), Youngs modulus E (in GPa) and compressibility (GPa^{-1}) for $LaAuO_3$ polymorphs. Subscript V indicates the Voigt bound, R indicates the Reuss bound and H indicates the Hill average.

Properties	**Phase**	
	α-$LaAuO_3$	β-$LaAuO_3$
C_{ij}	C_{11} = 294	C_{11} = 306
	C_{12} = 111	C_{12} = 124
	C_{13} = 148	C_{13} = 132
		C_{15} = 87
	C_{22} = 220	C_{22} = 397
	C_{23} = 129	C_{23} = 126
		C_{25}= 26
	C_{33} = 396	C_{33} = 271
		C_{35} = 47
	C_{44} =103	C_{44} =85
		C_{46} =11
	C_{55} =75	C_{55} =74
	C_{66} =78	C_{66} =80
B_V	188	193
B_R	173	141
B_H	180	167
G_V	86	87
G_R	82	73
G_H	84	80
E_x	216	169
E_y	161	318
E_z	292	197
Compressibility	0.006	0.007

In general, the elastic energy of a system subjected to an infinitesimal strain can be written as $U = \varepsilon_i C_{ij} \varepsilon_j$. The system is defined to be stable if $U > 0$ for every arbitrary strain ε. The elastic constant matrix C_{ij} is therefore required to be positive definite. This proposition is equivalent to any of the following [22].

1) The eigenvalues of C_{ij} are positive.

2) Every leading principal (or trailing) minor, including the determinant of C, is positive.

Table 3: The calculated eigenvalues and minors of elastic tensor for the studied phases.

Phase	**Leading Minors (GPa)**	**Eigenvalues (GPa)**
α-$LaAuO_3$	294 228 247	582 192 136
	199 163 144	103 74 77
β-$LaAuO_3$	306 325 276	601 246 157
	206 154 138	44 93 71

The second condition if also known as Sylvesters criterion. Analytical formula can be readily obtained from these conditions and are reported in literature for simple crystal structures. It is also possible to verify them numerically by means of computational linear algebra routines. This second approach has been followed in this work. The calculated eigenvalues and leading minors are reported in Table 3. For readability, we report the k^{th} root of each minor, where k is the minor's order. All the reported values are positive. We can therefore conclude that the investigated α- and β-$LaAuO_3$ phases are mechanically stable polymorphs. The experimental verification of the existence of the predicted beta phase would be a very interesting result.

Table 4: Calculated variations in the elastic moduli of $LaAuO_3$ polymorphs.

Young's modulus (GPa)			Linear compressibility (TPa^{-1})		Shear modulus (GPa)		Poisson's ratio	
	E_{min}	E_{max}	β_{min}	β_{max}	G_{min}	G_{max}	ν_{min}	ν_{max}
α-$LaAuO_3$	160.89	291.78	0.81764	3.1669	70.106	102.96	0.1593	0.4181
Anisotropy	1.814		3.8732		1.469		2.6249	
β-$LaAuO_3$	89.925	332.98	0.0449	6.1135	43.649	132.13	0.0918	0.8446
Anisotropy	3.703		136.16		3.027		9.2022	

The bulk modulus *B*, shear modulus *G*, Young's modulus *E* and Poisson's ratio *υ* can be assessed from the elastic stiffness moduli through the Voigt (*V*), Reuss (*R*) and Hill (*H*) approximations [23]. The *V* and *R* approximations usually give the upper and lower bounds, respectively, of these parameters as indicated in Table 2. Like the elastic-tensor, the bulk and shear moduli contain information regarding the hardness of a material with respect to various types of deformation. Properties such as bulk moduli, shear moduli, Young's moduli and Poisson's ratio can be computed from the values of elastic constants and the calculated values are tabulated in Table 2. There is strong anisotropy (Table 4; Figure 8) in the calculated shear moduli, Young modulus, linear compressibility and for Poisson's ratio in both α- and β-phase. This is associated with the presence of two dimensional AuO_4 chains along the (010) direction in these phases. The compressibility value of these polymorphs suggested that these polymorphs of $LaAuO_3$ are reasonably hard material. A parameter B/G is also introduced, in which B indicates the bulk modulus and G represent the shear modulus. The bulk and shear moduli are calculated from the Voigt–Reuss–Hill approximations [24- 26]. The high (low) B/G value is associated with ductility (brittleness) and the critical value which separates ductile and brittle [27] materials is 1.75. The calculated B/G values of $LaAuO_3$ polymorphs are larger than 1.75, implying the ductile nature of these materials.

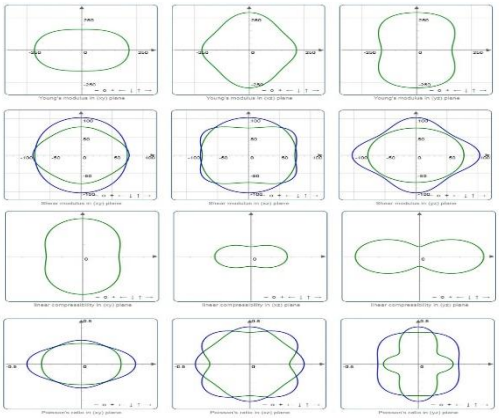

Figure 7: Spatial dependence of Young's modulus, shear modulus, linear compressibility and Poisson's ration of α-$LaAuO_3$. All plots were generated using the ELATE software [28].

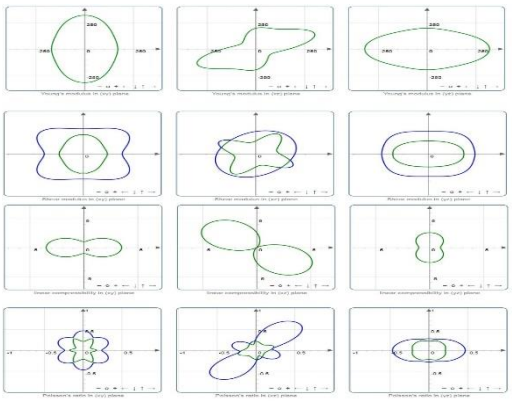

Figure 8: Spatial dependence of Young's modulus, shear modulus, linear compressibility and Poisson's ration of β-$LaAuO_3$. All plots were generated using the ELATE software [28].

Table 5: Calculated bandgap value of the $LaAuO_3$ system using GGA and HSE06 level.

Phase	GGA (eV)	HSE06 (eV)	Type of Bandgap
α-$LaAuO_3$	1.715	3.32	Indirect
β-$LaAuO_3$	0.817	2.2	Indirect

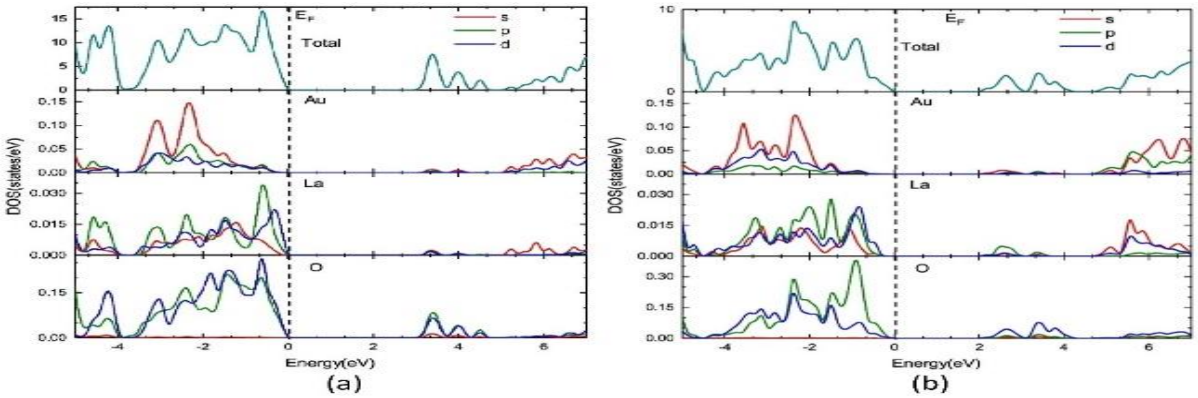

Figure 9: Total and site projected density of states (PDOS) of (a) α-$LaAuO_3$ and (b) β-$LaAuO_3$. The Fermi level is set to zero and marked by a vertical dotted line.

4.4 Electronic structure

The total density of states (DOS) at the equilibrium volume for the α- and DOS at the transition point for β-phase are displayed in Figure 10. Both phases exhibit a finite energy gap (Eg; 3.32 eV for α- and 2.20 eV for β-phase) between the valence band (VB) and the conduction band (CB) and hence, they are non-metals. It is well-known that standard functionals, such as the PBE-GGA, tend to underestimate band gaps. Hence, the obtained GGA values displayed in Table 6 are considerably smaller than the HSE06 values. It should be noted that the magnitude of the calculated bandgap value for the α-phase suggested that this compound might have the optical properties similar to technologically interesting compounds like ZnO (3.37 eV) and GaN From the PDOS of $LaAuO_3$, the distribution of various electronic states in the valence band and the conduction band can be characterized. The *d*- and *p*-states of O and *s*- and *d*-states of Au atoms are contribute dominantly to the valence band (VB). Both *s*-, *p*- and *d*-states of La atoms also contribute to the VB. The *p*- and d-states of La distributed energetically in the same range with O and *s*- and *d*-states and thus they can effectively overlap and form very strong covalent bonds. The *s*- and *d*-states of Au atoms are well localised and are mainly found below -1.5 eV. (3.39 eV). However, the energy conversion efficiency of the PV cell rate may be lower due to the indirect (ID) nature of the bandgap. Both polymorphs exhibit ID bandgap, as the valence band maximum (VBM) is found between Y- Γ (in α-) and Y (in β) while the conduction band minima (CBM) is between Y-Γ and Y-H, for α- and β-phase, respectively. However, we found that the electron/hole jump distance is minimum at Y- Γ for α-phase and Y-H for β-phase in the Brillouin zone. Moreover, the energy difference between the VBM and the band energy in the Y- Γ and Y-H, for α- and β-phase is less than 0.01 and 0.12 meV respectively. This makes it possible for this compound to function as a direct bandgap material. This indirect bandgap and its properties require further research to understand the working principle in real conditions [28].

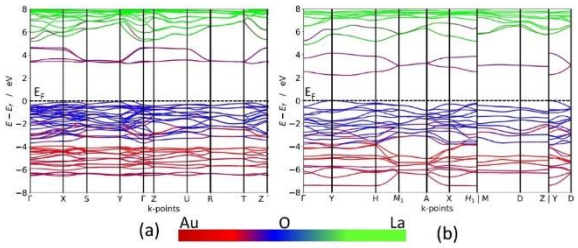

Figure 10: Calculated electronic band structure of (a) α- and (b) β-$LaAuO_3$ using HSE06 functional. The Fermi level is set to zero.

4.5 Activation energies for oxygen diffusion

In order to understand the possible application for the oxygen ion transport, we now analyse the possible diffusion pathways for O atoms in these studied systems. As a starting point, the vacancy formation energies are evaluated as $E_f = E_{tot}(n\text{-}1) - E_{tot}(n) - \mu$ where $E_{tot}(n)$ is the total energy of a system with *n*

oxygen atoms and μ is the chemical potential, taken to be one half of the total energy of an O_2 molecule. Suitable periodic repetitions of the original structures (supercells) are used to separate the point defect from its periodic repetition arising from the boundary conditions. We used 3×1×2 and 3×2×2 supercells for the orthorhombic and the monoclinic system respectively, corresponding to lattice parameters of at least 10 Å. The vacancy formation energies are found to be 1.85 eV and 1.99 eV for O_1 and O_2 respectively in the orthorhombic case, indicating a preference for an O_1 defect. In the monoclinic case, this trend is not

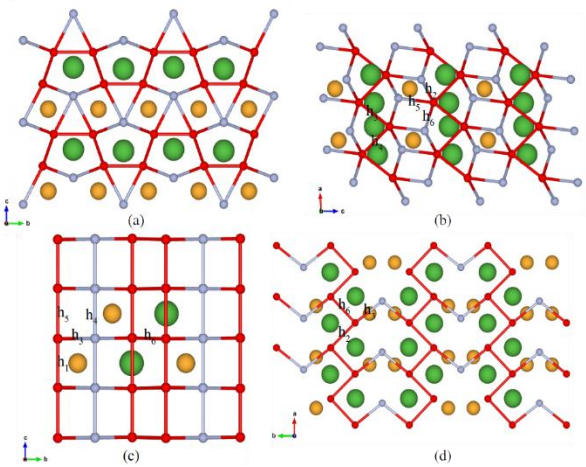

Figure 11: Oxygen framework indicated with ball-and-stick models for the monoclinic $LaAuO_3$ modification (a,b) and the orthorhombic one (c,d).

observed, as the formation energies are found to be 1.75 eV and 1.71 eV for the O_1 and the O_2 sites respectively. The activation energies are evaluated using the Nudged Elastic Band (NEB) method, using 5 intermediate images to model the transition path. The energy convergence threshold of each self-consistent calculation is set to 10^{-5} eV. The intermediate structures are optimised using the FIRE algorithm, with a force convergence threshold of 0.02 eV/Å, corresponding to energies converged within 10^{-3}eV for configurations at the saddle point. The Brillouin zone is sampled using a Gamma centered Monkhorst-Pack grid with a 0.3 $Å^{-1}$ spacing. The partial occupancies for each wave function are set according to the tetrahedron method with Blöchl corrections.

The oxygen network for the monoclinic modification is indicated in Figure 11. The possible nearest neighbour hops within a 3 Å cutoff are indicated using a stick to join the possible initial and final sites. Each hop is indicated by a h_n label. The number n is proportional to the length of the hop, reported in Table 1. The hops h_1, h_3, h_4 connect atoms of the O_1 type, whereas h_2, h_5 and h_6 connect O_1 atoms to O_2 ones. All the activation barriers, reported in Table 1, are found to be 1.40 eV or larger, making the diffusion of oxygen an unlikely process. The energy curves along the minimum energy paths are displayed in Figure 12. The largest activation energies are reported for h_2 and h_4. The global minimum energy path for oxygen diffusion is found to be in the *a*-plane, orthogonal to the *b* direction. This step is comprised of one h_1 hop followed by two h_6 ones, as clear from Figure 1, with an overall activation energy of about 1.50 eV. In the orthorhombic case, the diffusion of oxygen atoms is similarly found to be unlikely. The O network is indicated in Figure 11c and 3d. The h_1, h_2, h_5 and h_6 hops connect O_1 atoms, h_4 connects O_2 atoms and h_3 links the two inequivalent oxygen sites. As can be observed from Table 1, all the transitions including atoms of the O_2 type are energetically unfavorable. The linear diffusion of O_2 atoms involves an energy

barrier as large as 2.95 eV, whereas calculations for the h_3 hop did not yield any converged result. Diffusion of O_1 atoms is found to be more favorable. Two possible paths are available: the linear diffusion along the ***c*** direction, comprised by the h_1 and the h_5 hops and the zig-zag one along ***a***, comprised by h_2 and h_6. These paths are found to have activation energies of 1.65 eV and 1.38 eV respectively.

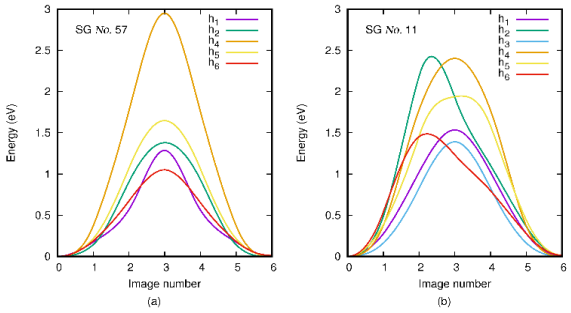

Figure 12: Energy along the minimum energy paths for the considered hops in the orthorhombic modification (a) and in the monoclinic one (b).

Table 6: Length for each of the considered nearest neighbors hops and corresponding activation energy barrier for the orthorhombic structure (left) and the monoclinic one (right).

	d **(Å)**	E_d **(eV)**	***d*** **(Å)**	E_d **(eV)**
h_1	2.83	1.29	2.72	1.53
h_2	2.86	1.38	2.79	2.43
h_3	2.87	-	2.82	1.39
h_4	2.88	2.95	2.84	2.4
h_5	2.92	1.65	2.9	1.95
h_6	2.94	1.05	2.94	1.49

Table 7: Calculated Raman and IR frequency (in cm^{-1}) for the Modes at the Γ Point of the Brillouin Zone for $LaAuO_3$ Polymorphs.

mode	***Pbcm*** **(57)**	***P121/m1*** **(11)**
Raman	A_g: 80, 132, 154, 179, 467, 518, 531, 765	A_g: 144, 175, 365,463, 509, 629, 726
	B_{1g}: 90, 130, 153, 168, 367, 467, 533, 719, 766	B_g: 271, 451, 530, 577, 698
	B_{2g}: 83, 214, 244, 451, 510, 688, 724	-
	B_{3g}: 140, 220, 427, 465, 517, 735,	-
IR	B_{1u}: 155, 326, 412, 433, 683, 697,	A_u: 111, 142, 158, 388, 579, 595, 654
	B_{2u} : 63, 119, 175,356, 402, 530, 709, 746,	B_u:136, 189, 240, 426, 464, 562, 645, 742
	B_{3u}: 107, 128, 417, 519, 585, 761	-

4.6 Vibrational spectroscopy

In general, the prepared samples from various methods often contain more than one phase (mixed phases), impurities and other crystal defects in such situations, we can use the theoretically simulated spectra, such as Raman and IR, to distinguish different phases within the sample. The theoretical studies on spectroscopic properties of materials will be therefore complementary to the experimental studies in the characterization of contaminated or multiphase samples. In connection with that, we have simulated the Raman and IR spectra. The phonon frequencies at the Γ point for the α- and β-$LaAuO_3$ phases are summarized in Table 7. According to the symmetry analysis (crystal point group), the optical modes at the Γ point can be classified into the following symmetry species for α- and β-$LaAuO_3$:

$\Gamma_\alpha = 8A_g(R) + 9B_{1g}(R) + 7B_{2g}(R) + 6B_{3g}(R) + 6B_{1u}(I) + 8B_{2u}(I) + 7B_{3u}(I)$

$\Gamma_\beta = 7A_g\,(R) + 5B_g\,(R) + 7A_u\,(I) + 8B_u\,(I)$

where the notations of R and I refer to Raman active and infrared active modes, respectively. To the best of our knowledge, there is no experimental Raman and IR data currently available for comparison. It may be noted that the calculated Raman frequencies using direct method for $NaAlH_4$ are found to be in good agreement with the corresponding experimental values within 5% error [29]. In general, the calculated Raman active phonon frequency values are underestimated with respect to corresponding experimental frequencies. We have displayed the simulated Raman and IR spectra for α- and β-$LaAuO_3$ in Figure 13,14 respectively. To have clarity in the Raman and IR spectrum, we have labelled only a limited number of peaks in Figure 13,14 and all the values are tabulated in Table 7.

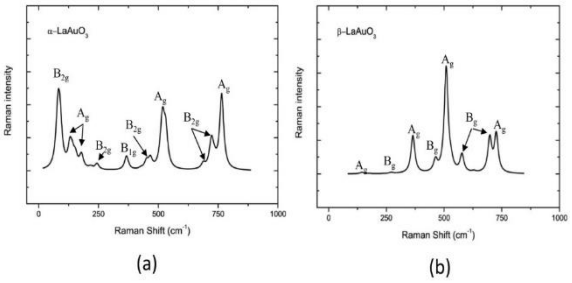

Figure 13: Theoretically simulated Raman spectra for α- and β-$LaAuO_3$ modifications at ambient conditions. For more clarity, only selected Raman active modes are marked in the Raman spectra.

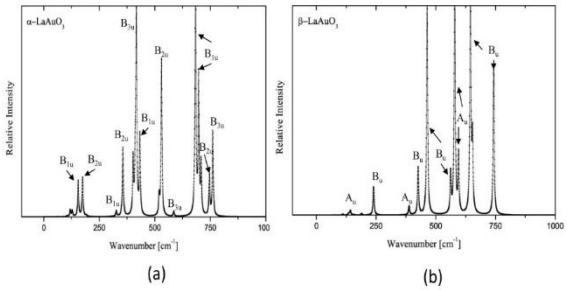

Figure 14: Theoretically simulated IR spectra for the α- and β-$LaAuO_3$ modifications at ambient conditions. For the β- phases, the spectra are simulated at the phase transition point (GPa). For more clarity, only selected IR active modes are marked in the α- and β-$LaAuO_3$ IR spectra.

The calculated zero-point energy (ZPE) for the α- and β-$LaAuO_3$ are 0.509 and 0.705 eV/f.u. (Table 9), respectively. The high-pressure phase has the higher ZPE values than the ambient phase this finding clearly indicates that the theoretically predicted transition pressure may be considerably deviate from the experimental measurements. Moreover, all our theoretical simulation we have assumed phase-pure sample with ideal structure where the temperature effect is not included. In the real case, however, the sample is comprehensive of impurities, defects and presence of more than one phase. This might make considerable difference in the phase transition pressure.

Table 8: Calculated Born-Effective-Charge Tensor Elements (Z) for the Constituents of $LaAuO_3$ polymorphs.

Compound	Position	*xx*	*Yy*	*zz*	*xy*	*xz*	*yx*	*yz*	*zx*	*zy*
α-$LaAuO_3$										
La	4*d*	4.39	4.8	4.76	-0.09	0	0.74	0	0	0
Au	4*d*	0.78	1.26	2.43	-1.17	0	-0.72	0	0	0
O1	*8e*	-2.12	-2.21	-2.64	0.46	0.534	-0.06	-0.42	0.2	-0.37
O2	4*c*	-0.93	-1.63	-1.9	0	0	0	-0.57	0	-0.4
β-$LaAuO_3$										
La	2e	4.32	4.32	3.85	0	-0.16	0	0	-0.1	0
Au	2*b*	2.13	1.93	1.34	1.1	0.6	0.49	-0.44	0.57	-0.88
O1	*4f*	-2.55	-2.02	-2	-0.44	-0.36	-0.21	0.19	-0.31	0.14
O2	2*e*	-1.35	-2.2	-1.18	0	0.28	0	0	0.15	0

4.7 Born effective charges and dielectric constants

The α- and β- polymorphs of $LaAuO_3$ are insulating crystals. For non-metallic crystals, the infrared optical modes at the Γ point are normally split into the longitudinal optical (LO) modes and transverse optical (TO) modes. This phenomenon, known as LO/TO splitting, is due to the long-range Coulomb interaction normally caused by the

displacement of atoms. The calculated dielectric constants for different polymorphs of $LaAuO_3$ are given in Table 9. The Born effective charges (BEC) are obtained from calculations of the Berry phase [30]. The BEC gives information about the amount of charge polarized by the application of the electric field. The King-Smith and Vanderbilt [30] method were used to calculate the polarizations in the perturbed cells and subsequently, the BEC tensor elements for the ions involved and the calculated BEC are tabulated in Table 8. For an ionic compound, the diagonal components of the effective charges in a Cartesian frame satisfy the relation $Z_{xx} = Z_{yy} = Z_{zz}$, whereas the off-diagonal components should be negligible. For the α- polymorph, the diagonal components of the effective charges at La and O_1 sites are almost equal ($Z_{xx} \approx Z_{yy} \approx Z_{zz}$). For the β-polymorph, on the other hand, the calculated diagonal component of the BEC is not symmetric ($Z_{xx} \neq Z_{yy} \neq Z_{zz}$). Some of the off-diagonal components are very small, but finite. In both α- and β- polymorphs, a similar BEC is found in Au and O_2 sites. The off-diagonal components are also not symmetric and have larger values. In general, for pure ionic systems, the calculated average BEC will be the same as that of the nominal ionic charge. But, for the studied α- and β-polymorphs, the calculated average BEC values clearly show that the bonding interaction deviates from the pure ionic case. Hence, the "average BEC charges" are deviating from the nominal ionic charges (2 for La, 3 for Au and 2 for O). Furthermore, the present study predicts that the BEC values are highly directional dependent for both Au and O_2 sites in the $LaAuO_3$ polymorphs, indicating the presence of finite covalent interaction. The components of the high- and low-frequency dielectric constant tensor, ε, were calculated, including local field effects, using the linear response method and are listed in Table 9. There are no experimental measurements for the $LaAuO_3$ polymorphs available for comparison. However, in our earlier study [31] we have demonstrated that one can reliably predict the dielectric constant within a few percentage deviations with respect to the experimental measurements. Hence, we conclude that the predicted ε values for the $LaAuO_3$ polymorphs (Table 9) are expected to be reliable.

Table 9: Components of the high- and low-frequency dielectric constant tensor ε and calculated zero-point energy (ZPE; eV/f.u.) for $LaAuO_3$ polymorphs.

	α-$LaAuO_3$	**β-$LaAuO_3$**
$\varepsilon^{\infty}_{xx}$	5.2	7.13
$\varepsilon^{\infty}_{yy}$	5.74	7.46
$\varepsilon^{\infty}_{zz}$	7.06	6.19
ε^{0}_{xx}	8.74	10.73
ε^{0}_{yy}	12.2	10.43
ε^{0}_{zz}	12.9	8.51
ZPE	0.509	0.705

4.8 Optical properties

The optical behavior of a compound has a major impact on its properties for photovoltaic applications. The central quantity of the optical properties is the dielectric function ε(ω), which describes the linear response of the system to an electromagnetic radiation, governing the propagation of radiation in a medium. Here, ε(ω) is connected with the interaction of photons with electrons. Its imaginary part $\varepsilon_2(\omega)$ can be derived from interbond optical transitions by calculating the momentum matrix elements between the occupied and unoccupied states within the selection rules and its real part $\varepsilon_1(\omega)$ can be derived from $\varepsilon_2(\omega)$ by the Kramer–Kronig relationship [32]. The real part of ε(ω) in the limit of zero energy (or infinite wavelength) is equal to the square of the refractive index n(ω). All the frequency dependent optical properties, such as refractive index n(ω), extinction coefficient k(ω), absorption coefficient α(ω), optical conductivity σ(ω), reflectivity R(ω) and electron energy-loss spectrum L(ω) can be deduced from $\varepsilon_1(\omega)$ and $\varepsilon_2(\omega)$ [33].

The calculated real and imaginary part of the dielectric function and absorption coefficients of polycrystalline α- and β- $LaAuO_3$ polymorphs are

presented in Figure 15. Even though there are some differences in the optical properties between α- and β-$LaAuO_3$, the global shape of the optical properties for both polymorphs are similar. There are three main regions in the $\varepsilon_2(\omega)$ plot (Figure 15a) of α- and β-$LaAuO_3$ polymorphs. The first region is located between ca. 3 to 6.5 eV, the second region is between ca.7.5 eV to 11.0 eV and the third region is at higher energy, between 18 and 25 eV. The real part of dielectric function $\varepsilon_1(\omega)$ (Figure 15 a) allows us to estimate the value of the refractive index at infinite wavelength is 2.3 for 2.55 for α- and β- $LaAuO_3$, respectively. At the low frequency (0– 3.6 eV), the imaginary part $\varepsilon_2(\omega)$ is zero below the bandgap, which is consistent with the order of bandgap.

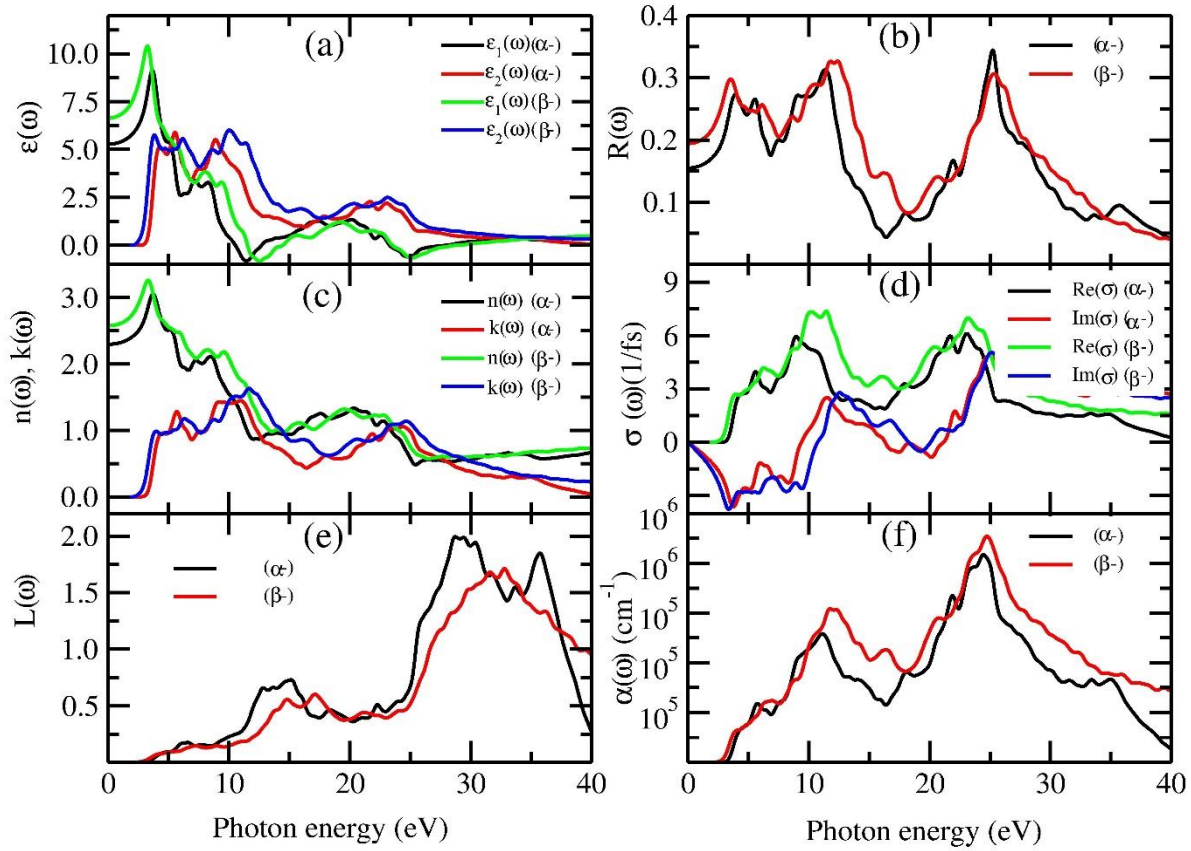

Figure 15: Calculated optical properties for α-$LaAuO_3$ and β-$LaAuO_3$: (a) dielectric function ε(ω), (b) reflectivity *R*(ω), (c) refractive index *n*(ω); extinction coefficient *k*(ω), (d) optical conductivity σ(ω), (e) energy loss function *L*(ω) and (f) absorption α(ω).

The reflectivity spectrum and extinction coefficient k(ω) (the imaginary part of the complex refractive index) of different polymorphs of $LaAuO_3$ are shows in Figure 15b and c respectively. The reflectivity spectrum has major peaks for α-phase at ca. 4.1, 5.4, 11.5 and 25 eV and for β-phase at 3.7, 6.1, 12.1 and 25 eV. The reflectivity at infinite wavelength is ca. 0.15 and 0.2 for α- and β-$LaAuO_3$, respectively. $LaAuO_3$ has a finite value for the reflectivity R(ω), (Figure 15b) in the range 2.8–32 eV. The optical conductivity σ(ω) plot of $LaAuO_3$ polymorphs are shown in Figure 15d. The real part of the complex conductivity has three main peaks at ca. 10 and 21 eV, respectively.

The electron energy-loss function L(ω) (Figure 15e) is an important optical parameter describing the energy loss of a fast electron traversing in a certain material. The peaks in the L(ω) spectra represent the characteristics associated with the plasma resonance and the corresponding frequency is the so-called plasma frequency, above which the material is a dielectric [$\varepsilon_1(\omega) > 0$] and below which the material behaves like a metallic compound in some sense [$\varepsilon_1(\omega) < 0$]. In addition, the peaks of the L(ω) spectra

overlap the trailing edges in the reflection spectra. There are three peaks of L(ω) of α-$LaAuO_3$ [first in the 11.3 to 16.7 eV range, the second in the 24 to 32 eV range and third in the 34 to 37 eV range] and two peaks for the β-phase[first region in the 12 to 19 eV range and the second region in the 25 to 37 eV range], corresponding to the reduction of R(ω). Both α- and β- polymorphs of $LaAuO_3$ has an absorption band (Figure 15f) from 2.8 to 40 eV, which contains two regions [first region between 2.8 to 15 eV and second region between 19 to 30 eV].

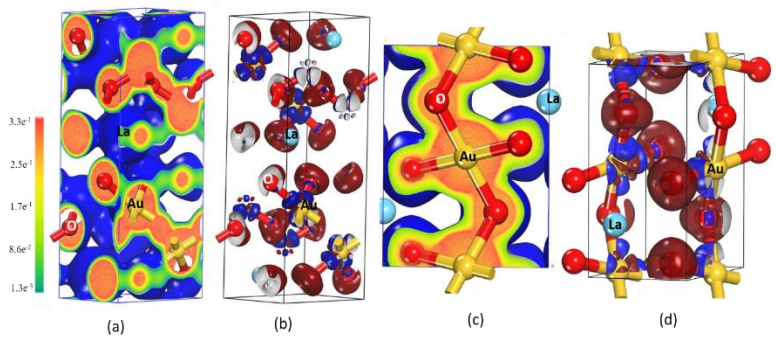

Figure 1: Calculated charge density (a and d) and charge transfer (b and e; isosurface value -0.1 is given in blue and +0.1 value represented as dark brown) plots for α- and β-$LaAuO_3$.

4.9 Chemical bonding

The α- and β- $LaAuO_3$ exhibit similar features and in view of that we have documented the charge density and charge density difference for α- and β- $LaAuO_3$. Figure 16a and d show the charge-density distribution at the La, Au and O sites, from which it is evident that the highest charge density resides in the immediate vicinity of the nuclei. Furthermore, the spherical charge distribution shows that the bonding interactions between La–O have predominantly an ionic character. On the other hand, in the interactions between Au–O is predominantly directional. The substantial difference in the electro-negativity between La and O/Au suggests the presence of strong ionic character (i.e., the O valence electrons transferred to the La/Au sites) and a significant difference in the electronegativity between Au and O suggests the presence of covalent character. From the charge transfer plot (the difference between the electron density of the compound and the electron density of the constituent atoms), one can obtain insight on redistribution of electrons when the solid is formed. This allows one to see how the actual chemical bond is formed in real space. To depict the role of charge transfer, we have displayed the charge transfer plot for α- and β- $LaAuO_3$ in Figure 16b and e, respectively. From Figure 16, it is clear that electrons are transferred from La to the O site. So, there is considerable ionic bonding component present between La and O. Due to the presence of considerable covalent bonding, the charge depletion at the Au site is not spherically symmetric (Figure 16b,e).

In order to quantify the bonding and estimate the amount of electrons on and between the participating atoms, we have computed the Mulliken-population. Although there is no unique definition to identify the number of electrons associated with an atom in a molecule or an atomic grouping in a solid, it has nevertheless proved useful in many cases to perform population analyses. Due to its simplicity, the Mulliken-population [34] scheme has become the most popular approach. However, the method is more qualitative than quantitative, providing results that are sensitive to the atomic basis. The calculated Mulliken charges are reported in Table 10 for α- and β-$LaAuO_3$ polymorphs. For the studied $LaAuO_3$ polymorphs the MEC value for the La is +1.91. This finding is

consistent with the charge density analyzes and the magnitude of the MEC shows that La does not completely donate its three valence electrons to the Au and O atoms, which is much smaller than in a pure ionic picture. To understand the bonding interaction between the constituents, the bond overlap population (BOP) values are calculated on the basis of Mulliken population analysis. The BOP values can provide useful information about the bonding property between atoms. A high BOP value indicates a strong covalent bond, while a low BOP value indicates an ionic interaction. The calculated BOP values for the $LaAuO_3$ polymorphs are displayed in Table 10. The BOP values for the La–O bonds in the calculated two structures are vary between 0.15 to 0.4. Similarly, the calculated BOP values for the Au–O bonds vary between 0.35 and 0.43. Therefore, the La–O bonds in these $LaAuO_3$ polymorphs have dominant ionic character, whereas the Au–O interaction have noticeable covalent character. When we compare the BOP values for the different bonding interaction between atoms in α- and β- phases; overall the bonding interactions are similar in both phases.

Table 10: The Mulliken population charge density analysis for α- and β-$LaAuO_3$ polymorphs are given in terms of bond overlap population (denoted as BOP) and Mulliken-effective charges (MEC) (given in e).

Properties	Component	α-$LaAuO_3$	β-$LaAuO_3$
MEC	La	1.91	1.91
	Au	0.29	0.24
	O1	-0.76	-0.74
	O2	-0.7	-0.67
BOP	Au-O	0.35-0.41	0.39-0.43
	La-O	0.13-0.38	0.15-0.40

5. Conclusion

The structural phase stability, electronic structure, thermodynamical, mechanical, spectroscopic and optical properties of $LaAuO_3$ in two different polymorphs have been studied by state-of-the-art density-functional theory calculations. The ground-state crystal structure and equilibrium structural parameters of $LaAuO_3$ have been predicted from structural optimization with 12 distinct structures as input using force as well as stress minimizations. At ambient condition $LaAuO_3$ crystallises in orthorhombic (Pbcm) phase and at 1.98 GPa pressure it transforms in to monoclinic structure (space group $P2_1/m$). The layered nature of the structural arrangement suggests a large O-ion conductivity. However, NEB simulation revealed that both polymorphs exhibit a sluggish diffusion of O-ions. The phonon density of states at the equilibrium volume for these two polymorphs are calculated using perturbation theory, revealing that the predicted phases are dynamically stable. Similarly, the calculated single crystal elastic constants revealed that the predicted phases fulfil the mechanical stability criteria. For the experimental verification in future studies, we have simulated the Raman and IR spectra. The calculated electronic structures at HSE06 level reveal that $LaAuO_3$ is an indirect band gap semiconductor with estimated band gap of 3.32 and 2.20 eV for α-$LaAuO_3$ and β-$LaAuO_3$, respectively. The calculated Born effective and Mulliken effective charge analyses and charge density, confirm that the chemical bonding character of $LaAuO_3$ polymorphs is predominantly ionic with noticeable covalent character.

6. Acknowledgment

The authors gratefully acknowledge the Research Council of Norway for providing the computer time (under the project number NN2875k) at the Norwegian supercomputer. PV gratefully acknowledge Dr. S Kumar for fruitful discussions.

Data availability: All the ab initio data are freely available to the public as part of the DFTBD database (link http://folk.uio.no/ponniahv/Database/index.htm)

References

1. AJ Freeman. Materials by design and the exciting role of quantum computation/simulation. J Computational Applied Mathe. 2002; 149: 27-56.

2. D Xiao, W Zhu, Y Ran, N Nagaosa, S

Okamoto. Interface engineering of quantum Hall effects in digital transition metal oxide heterostructures. Nature Communications. 2011; 2: 596.

3. S Okamoto, W Zhu, Y Nomura, R Arita, D Xiao, Naoto Nagaosa. Correlation effects in (111) bilayers of perovskite transition-metal oxides. Physical Review B 2014. 89:195121.

4. G Kresse, J Furthmuller. Efficiency of ab-initio total energy calculations for metals and semiconductors using a plane-wave basis set. Computational Materials Science. 1996; 6: 15-50.

5. G Kresse, J Furthmüller. Efficient iterative schemes for ab initio total-energy calculations using a plane-wave basis set. Phys. Rev. B 1996. 54:11169-11186.

6. JP Perdew, K Burke, M Ernzerhof. Generalized Gradient Approximation Made Simple. Phys Rev Letters. 1996; 77: 3865-3868.

7. P Vinet, JH Rose, J Ferrante, JR Smith. Temperature effects on the universal equation of state of solids. J Phys Condens Matter. 1989; 1: 1941–1963.

8. A Togo, F Oba, I Tanaka. First-principles calculations of the ferroelastic transition between rutile-type and SiO_2 at high pressures. Phys Rev B. 2008; 78: 134106.

9. HJ Monkhorst, JD Pack. Special points for Brillouin-zone integrations. Phys Rev B. 1976. 13: 5188-5192.

10. Inorganic Crystal Structure Database (ICSD).

11. M Ralle, M Jansen. Synthesis and Crystal Structure Determination of $laAuO_3$. J. Solid State Chem. 1992; 105: 378-384.

12. JP Attfield , G Férey . Structural correlations within the lanthanum palladium oxide family. Journal of Solid State Chemistry. 1989; 80: 286-298.

13. A Seko , A Togo , F Oba , I Tanaka. Structure and Stability of a Homologous Series of Tin Oxides. Phys Rev Letters. 2008; 100: 045702.

14. VB Deyirmenjian, V Heine, MC Payne, V Milman, RM Lynden-Bell, MW Finnis. Ab Initio Atomistic Simulation of the Strength of Defective Aluminum and Tests of Empirical Force Models. Phys Rev B. 1995; 52: 15191-15207.

15. M Marlo, V Milman. Density-functional study of bulk and surface properties of titanium nitride using different exchange-correlation functionals. Phys Rev B. 2000; 62: 2899-2907.

16. V Milman, MC Warren. Elastic properties of TiB_2 and MgB_2. J Phys Condens Matter. 2001; 13: 5585-5595.

17. P Ravindran, P Vajeeston, R Vidya, A Kjekshus, H Fjellvåg. Detailed electronic structure studies on superconducting MgB_2 and related compounds. Phys Rev B. 2001; 64: 224509.

18. A de Vita , I Manassidis, JS Lin, MJ Gillan. The energetics of Frenkel defects in Li_2O from 1st principles. Europhys Lett. 1992; 19: 605-610.

19. P Ravindran, L Fast, PA Korzhavyi, B Johansson. Density functional theory for calculation of elastic properties of orthorhombic crystals: Application to $TiSi_2$. J Appl Phys. 1998; 84: 4891-4904.

20. VB eyirmenjian, V Heine, MC Payne, V Milman, RM Lynden-Bell, MW Finnis. Ab initio atomistic simulation of the strength of defective aluminium and tests of empirical force models. Phys Rev B. 1995; 52: 15191-15207.

21. J Haines, J Leger, G Bocquillon. Synthesis and Design of Superhard Materials. Annu. Rev Mater Res. 2001; 31: 1-23.

22. RA Horn, CR Johnson. Matrix Analysis. Cambridge University Press: 2012.

23. JP Watt. Hashin-Shtrikman bounds on the effective elastic moduli of polycrystals with orthorhombic symmetry. J Appl Phys. 1980; 51: 1520.

24. A Reuss. Berechnung der Fließgrenze von Mischkristallen auf Grund der Plastizitätsbedingung für Einkristalle. ZAMM - Journal of Applied Mathematics and Mechanics / Zeitschrift für

Angewandte Mathematik und Mechanik. 1929; 9: 49-58.

25. Hill R. The Elastic Behaviour of a Crystalline Aggregate. Proc. Phys Soc London. 1952; 65: 349-354.

26. Voigt W. Lehrbuch der Kristallphysik. Leipzig. 1928.

27. SF Pugh. Relations between the elastic moduli and the plastic properties of polycrystalline pure metals. Philos Mag. 1954; 45: 823-843.

28. G Romain G, P Pluton, François-Xavier C. ELATE: an open-source online application for analysis and visualization of elastic tensors. Journal of Physics: Condensed Matter. 2016; 28: 275201.

29. X Ke, A Kuwabara, I Tanaka. Cubic and orthorhombic structures of aluminum hydride AlH3 predicted by a first-principles study. Phys Rev B. 2005; 71: 184107.

30. RD King-Smith, D Vanderbilt. Theory of polarization of crystalline solids. Phys Rev B. 1993; 47: 1651-1654.

31. P Vajeeston, P Ravindran, H Fjellvåg. Phonon IR, Raman Spectra, NMR Parameters and Elastic Constant Calculations for AlH_3 Polymorphs. The Journal of Physical Chemistry A. 2011; 115: 10708-10719.

32. L-M Yang, P Vajeeston, P Ravindran, H Fjellvåg, M Tilset. Revisiting isoreticular MOFs of alkaline earth metals: a comprehensive study on phase stability, electronic structure, chemical bonding and optical properties of A–IRMOF-1 (A = Be, Mg, Ca, Sr, Ba). Physical Chemistry Chemical Physics. 2011; 13: 10191-10203.

33. PY Yu, M Cardona. Fundamentals of Semiconductors. Springer-Verlag: Berlin. 1996.

34. RS Mulliken. Electronic Population Analysis on LCAO–MO Molecular Wave Functions. J Chem Phys. 1955.

Citation: P Vajeeston, Department of Chemistry, Center for Materials Sciences and Nanotechnology, University of Oslo, P.O. Box 1033 Blindern, N-0315 Oslo, Norway.

Copy Right: © 2019 P Vajeeston. This is an open-access article distributed under the terms of the Creative Commons Attribution License, which permits unrestricted use, distribution and reproduction in any medium, provided the original author and source are credited.